Supporting Information

A bioinspired solar evaporator for continuous and efficient desalination by salt dilution and secretion

Shuqian Zhang,[a] Yang Yuan,[a] Wang Zhang,*[a] Fang Song,[a] Jinghan Li,[a] Qinglei Liu,[a] Jiajun Gu,[a] Di Zhang,*[a]

[a] State Key Laboratory of Metal Matrix Composites, School of Materials Science and Engineering, Shanghai Jiao Tong University, Shanghai 200240, P.R.China

Email addresses: wangzhang@sjtu.edu.cn, zhangdi@sjtu.edu.cn

Supplementary Notes

Note S1. Chemicals and materials

Pyrrole (C_4H_5N) and Iron (III) chloride hexahydrate ($FeCl_3 \cdot 6H_2O$) were purchased from Shanghai Aladdin Bio-Chem Technology Co., Ltd. Ethanol, Sodium chloride (NaCl), methyl orange, methylene blue and rhodamine B were purchased from Sinopharm Chemical Reagent Co., Ltd. Artificial seawater was purchased from China Fanying Corporation. Glass fiber cloth and glass fiber felt were fabricated from China Jushi Co., Ltd. Filter paper was purchased from Shanghai Titan Technology Co., Ltd. All reagents were used as received without further purification. Redistilled water was used for all the solution. The acidity, mineral and organic content conditions were tested with water testing kits provided by Beijing Mingde Kangce Science & Technology Co. Ltd.

Note S2. Characterizations

The 3D images of PPy/GFF and detached salt were characterized by an X-ray microscope (Xradia 520 Versa). The morphology of sample was characterized by 3D microscope with super depth of field (VHX-1000E) and field emission scanning electron microscope (Mira3, accelerating voltage 10 kV). The XPS results were collected by X-ray photoelectron spectroscopy (AXIS Ultra DLD) with an Al Kα source. The FTIR spectra were measured by a Micro-imaging Fourier transform infrared spectrometer (NicoletiN10 MX). The thermogravimetric curves were recorded by a thermogravimetric analyzer (Pyris 1 TGA). The UV-vis-NIR spectra were recorded on a UV-vis-NIR spectrophotometer (Perkin Elmer, lambda 750s). Water transport measurements were carried out using a contact angle device (JC2000, Shanghai Zhongchen, China). The thermal conductivities of PPy/GFF in the dry and wet state were measured by the thermal conductivity measuring instrument (Hot Disk TPS 2500s). The infrared thermal photographs were captured by

an IR camera (FLIR T620). The temperature above the absorber and temperature changes of samples and the bulk water was captured by the thermocouples (YA204R/C2/U/TP1). The water storage mass of samples and mass of GFF before and after PPy coating were measured by an electronic scale (BSM-220.4). In-plane water transport results were recorded by the SLR camera (Canon DS126281). The ion concentration of artificial seawater and collected clean water were collected by inductively coupled plasma atomic emission spectrometry (Thermo iCAP6000). The concentration of methylene blue and methyl orange was 10 mg L^{-1} and 56 mg L^{-1}, respectively.

Note S3. Optical absorption calculation

The absorption was calculated from A=1-R-T, where R and T are the reflection and transmission of the samples, respectively. The absorption values of different samples were calculated based on the Equation S1:

$$\alpha = \frac{\int_{280}^{2500} I(\lambda) A(\lambda) d\lambda}{\int_{280}^{2500} I(\lambda) d\lambda} \quad \text{(S1)}$$

Note S4. Solar evaporation experiment

A typical lab-made system was applied in the solar evaporation experiment. The sample (2×2 cm) was placed on the surface of the air-laid paper which was wrapped around a PS foam that floated on the water in a glass breaker and functioned as a 2D water transport pathway. The rest region was covered by a piece of aluminum foil. The samples were irradiated by a solar simulator (Newport 94023A, Class AAA) and the simulated sunlight intensity was calibrated by an optical power meter (Thorlabs PM100D). The same solar illumination intensity was applied for all tests. The real-time mass changes were recorded by an electronic scale (BSM-220.4) connected to the computer. The salt secretion bundles were radically placed with a diameter of 4 cm. The time-lapse

images and videos of salt creeping were captured by a smartphone. The ambient temperature was controlled at about 25 °C, and the relative humidity was about 50% during test.

Note S5. Water evaporation efficiency (η)

The evaporation rate was calculated according to the linear fitting result from the mass change curves of water with time. The evaporation efficiencies were calculated based on the Equation S2:

$$\eta = \frac{m h_{LV}}{C_{opt} P_0} \tag{S2}$$

where m is the water evaporation rate subtracted by the value in dark area ($m = m_{light} - m_{dark}$, m_{dark} = 0.18 kg m^{-2} h^{-1} in this study), P_0 is the nominal solar irradiation value of 1 kW m^{-2}, C_{opt} represents the optical concentration, h_{LV} is the total enthalpy of liquid-steam phase change. h_{LV} includes the sensible heat of water and the phase-change enthalpy and can be calculated using the Equation S3:

$$h_{LV} = c\Delta T + \Delta h \tag{S3}$$

where is c the specific heat capacity of water (4.2 kJ kg^{-1} K^{-1}). For example, under one sun illumination, ΔT is the temperature increase of water from 25 ℃ to ~38 ℃ as shown in Fig. S7 and Fig. S12, and the Δh is the phase-change enthalpy at the temperature of evaporation surface (2410 kJ kg^{-1} at ~38 ℃). Thus, h_{LV} is calculated to be 2466 kJ kg^{-1}. The efficiencies under different sun irradiation were calculated in the same way. The temperatures and h_{LV} under different sun irradiation were shown in Fig. S8 and Table S2.

Note S6. Heat loss analysis

The heat loss of the solar evaporator through three forms: (1) radiation (2) convection and (3) conduction. The details of analysis are shown below.

Radiation:

The radiation loss was calculated by Stefan-Boltzman equation:

$$\phi=\varepsilon A\sigma(T_1^4-T_2^4) \quad \text{(S4)}$$

where ϕ represents the heat flux, ε is the emissivity (~0.95), A denotes the evaporation surface area (4 cm^2), σ is the Stefan-Boltzman constant (5.67×10^{-8} W m^{-2} K^{-4}), T_1 is the average temperature of evaporation surface (~ 38 ℃) at a steady condition, T_2 is the ambient temperature (~32 ℃) above the absorber as shown in Fig. S9. According to the Equation S4, the radiation heat loss is calculated to be ~3.8 % under one sun illumination.

Convection:

The convection loss was calculated by Newton's law of cooling:

$$Q=hA\Delta T \quad \text{(S5)}$$

where Q represents the heat, h is the convection heat transfer coefficient (5 W m^{-2} K^{-1}), A is the surface area (4 cm^2), ΔT denotes the difference between the surface temperature and ambient temperature above the absorber. Based on the Equation S5, the convection heat loss is 3%.

Conduction:

The conduction heat loss is the heat transferred directly from the absorber to the bulk water.

$$Q=cm\Delta T \quad \text{(S6)}$$

where Q denotes the heat, c is the specific heat capacity of water (4.2 kJ kg^{-1} K^{-1}), m represents the weight of bulk water, ΔT is the increased temperature of bulk water caused by heat transferred from the absorber. In this work, the conduction heat can be ignored due to the low thermal conductivity of samples and the thermal insulation management.

Based on the analysis above, the total heat loss is ~6.8% and the rest energy was used for reflection (2.6%) and water evaporation (~ 90.6%).

Supporting Figures

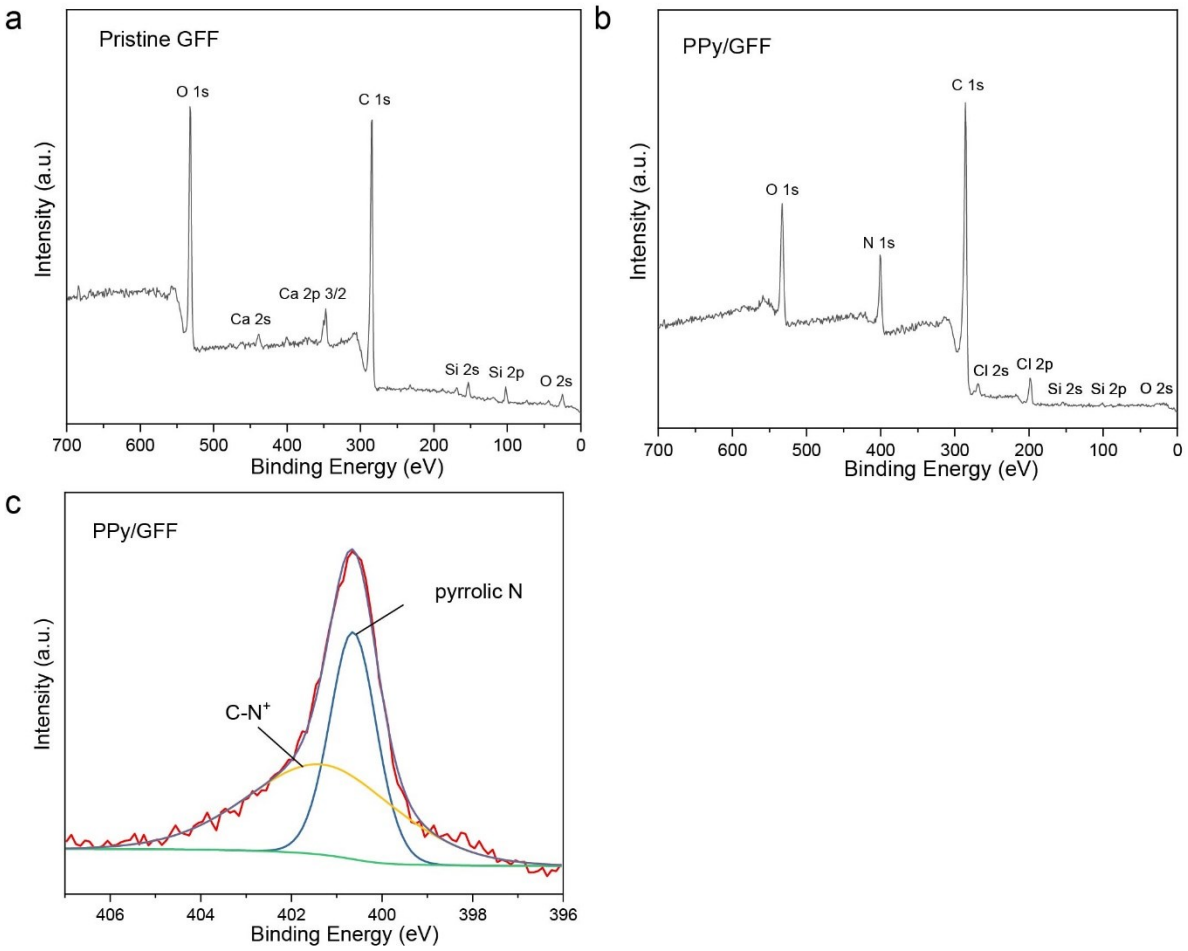

Fig. S1 XPS spectra of pristine GFF and PPy/GFF. XPS full scan spectra of (a) pristine GFF, (b) PPy/GFF. (c) High-resolution N 1s spectra of PPy/GFF.

X-ray photoelectron spectroscopy (XPS) was performed to investigate the elemental composition of GFF and PPy/GFF. Apart from the obvious signal of Na, O, Ca, C, Si, elements in pristine glass fibers, N (10.52 at%) and Cl (2.04 at%) can be found in the sample after PPy coating. The Cl element was introduced from Iron (III) chloride hexahydrate. The high-resolution XPS spectrum of N 1s can be deconvoluted into pyrrolic N (400.6 eV) and C-N^+(401.2 eV).

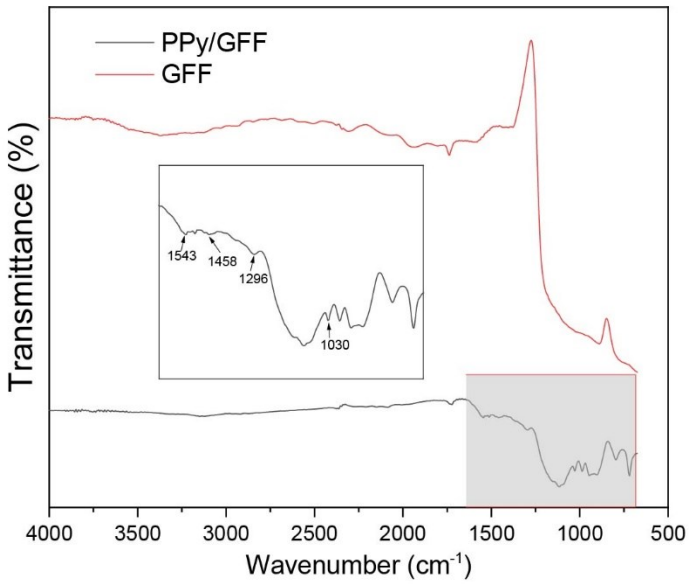

Fig. S2 FTIR spectra of pristine GFF and PPy/GFF. The inset is the partial enlarged view of PPy/GFF, indicating the characteristic peaks.

The characteristic peaks of 1543, 1458, 1296 and 1030 cm^{-1} in FTIR spectrum of PPy/GFF represent C-C/C=C stretching, vibration of pyrrole ring, C-N stretching vibration, and the in-plane deformation of N–H bonds, respectively, proving the existence of PPy.

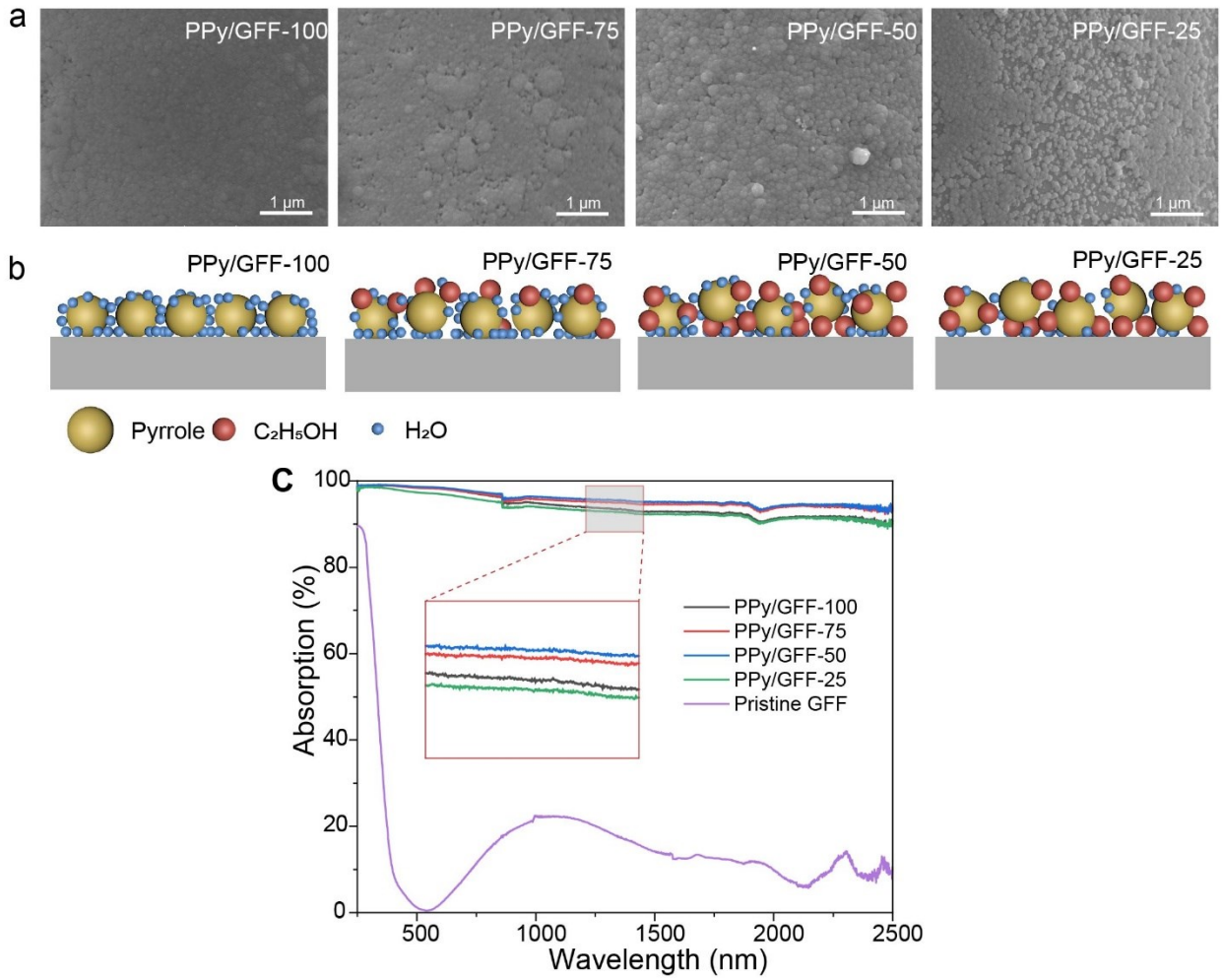

Fig. S3 Morphological control of PPy layers. (a) Magnified SEM images of PPy/GFF fabricated with decreasing volume ratios of water to ethanol in the pyrrole solution. (b) Schematic diagram of intermolecular binding among pyrrole, water, ethanol and glass fiber. (c) Solar absorption spectra of PPy/GFF and pristine GFF. The inset is the partial enlarged view.

The volume ratios of water to ethanol in the precursor solution were 100:0, 75:25, 50:50, 25:75, and the samples were named as PPy/GFF-100, PPy/GFF-75, PPy/GFF-50, PPy/GFF-25, respectively. As water decreased, the coating became rougher until the PPy particles failed to completely cover the surface (Fig. S3a). This probably results from the strength of intermolecular forces among pyrrole, water, ethanol, and glass fiber (Fig. S3b). When the solvent for the precursor

was pure water, pyrrole was uniformly absorbed on the glass fiber and then oxidized to uniform PPy film. When the solvent was the mixture of water and ethanol, compared with water, ethanol molecules had weaker binding force with glass fiber and stronger binding force with pyrrole. Hence, the pyrrole was staggered-arranged on the surface of glass fiber and the coating after oxidation was rougher with the ethanol content increasing in the precursors. For higher ethanol concentration (PPy/GFF-25), it is difficult for pyrrole to attach to glass fiber. The rougher PPy coating is more beneficial to reduce the specular light reflection and enhance solar absorption (Fig. S3c). Thus, the optical absorption of the PPy/GFF increased first with the water content decreasing in precursors, and the PPy/GFF-50 had the highest light absorption of 97.4%. The light absorption of PPy/GFF-25 decreased since the surface was not completely covered by PPy particles.

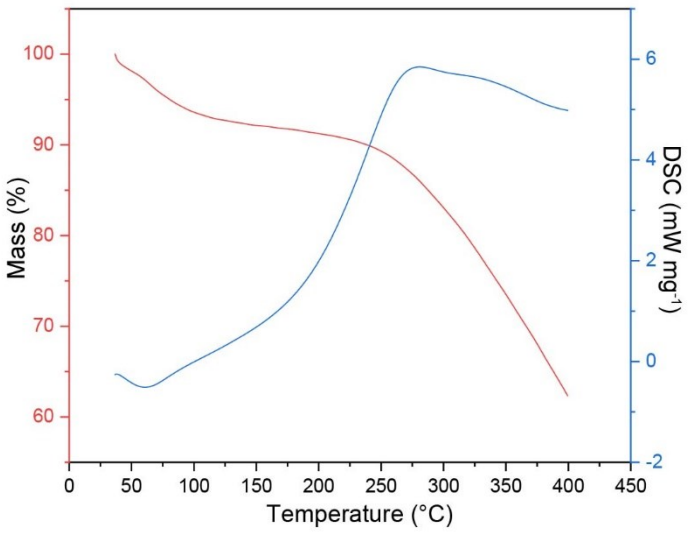

Fig. S4 Thermogravimetric curves of PPy powder.

The decomposition temperature of PPy is 283 °C, much higher than the boiling point of water.

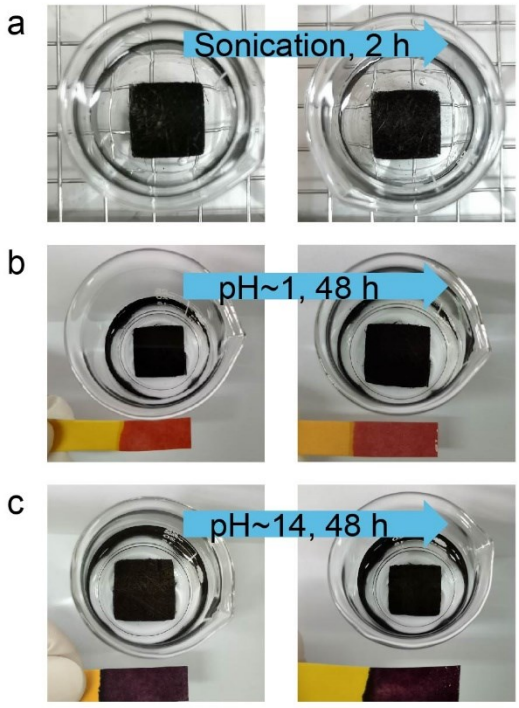

Fig. S5 Mechanical stability of the PPy/GFF under a series of harsh conditions. (a) ultrasonic agitation (200 W, 2 h), (b) acidic (pH~1, 48 h) and (c) alkaline (pH~14, 48 h).

The PPy/GFF maintained intact without any breakage after a series of harsh conditions.

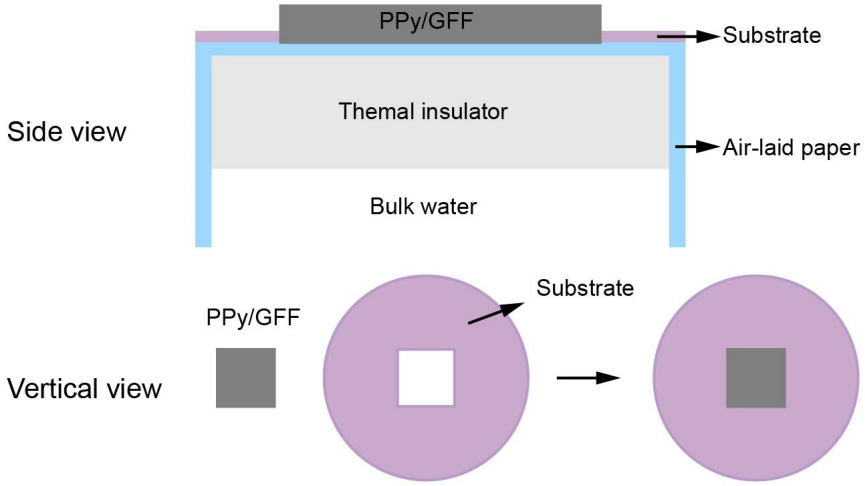

Fig. S6 Scheme of the PPy/GFF for solar steam generation.

The PS foam functions as the stand and thermal insulation layer to avoid the direct contact between the absorber and the bulk water. PS foam is covered with a piece of air-laid paper that can transport water from bulk to evaporation surface. The absorber is placed on the air-laid paper, with the rest area covered by aluminum foil.

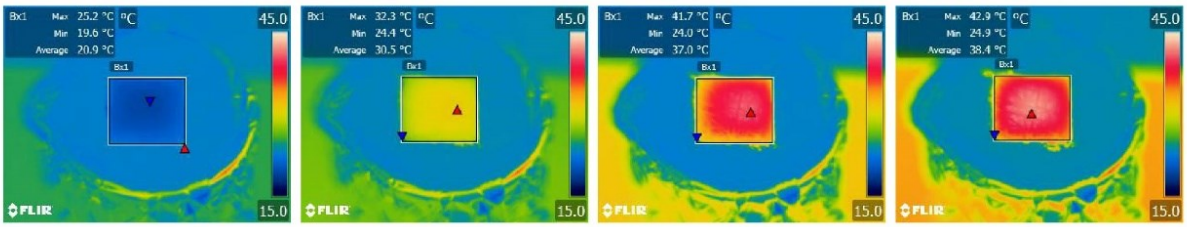

Fig. S7 Infrared thermal images of the PPy/GFF during the solar evaporation for 1 h under one sun irradiation.

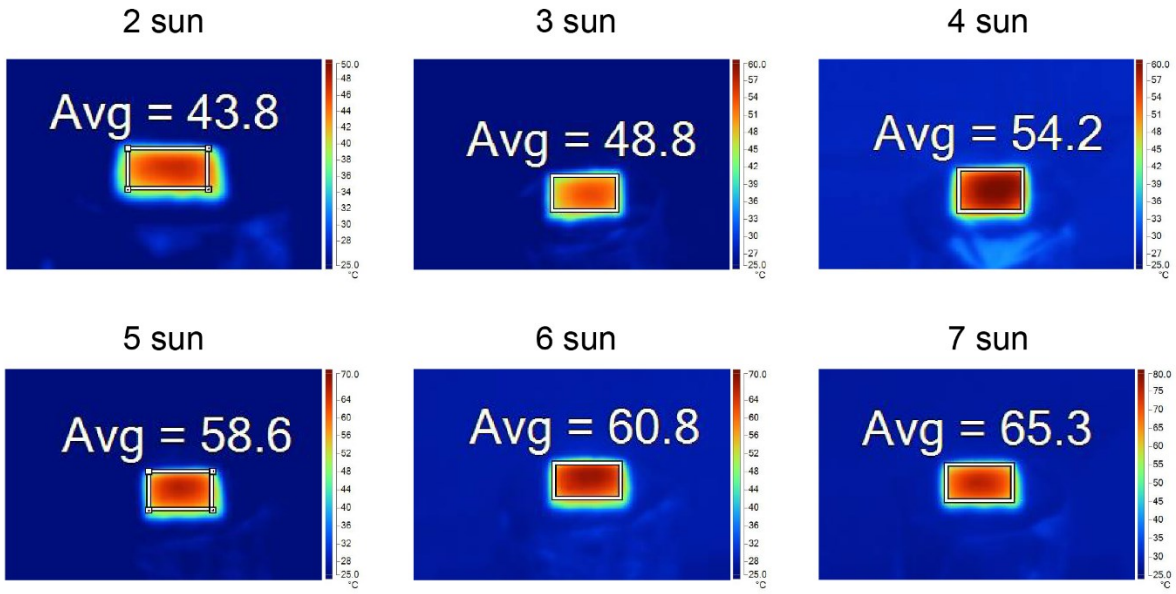

Fig. S8 Infrared thermal images of the PPy/GFF during the solar evaporation for 1 h under different sun irradiation.

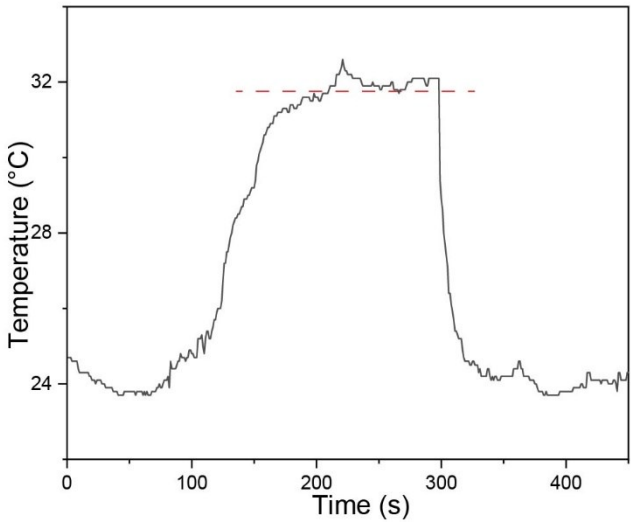

Fig. S9 Ambient temperature under one sun illumination above the evaporator captured by the thermocouple.

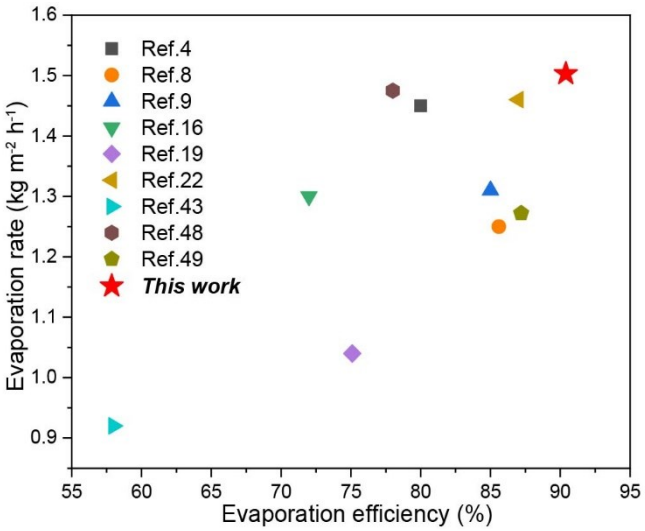

Fig. S10 Solar evaporation rates and efficiencies of PPy/GFF compared to recently reported high-performance solar evaporators. [4,8,9,16,19,22,43,48,49]

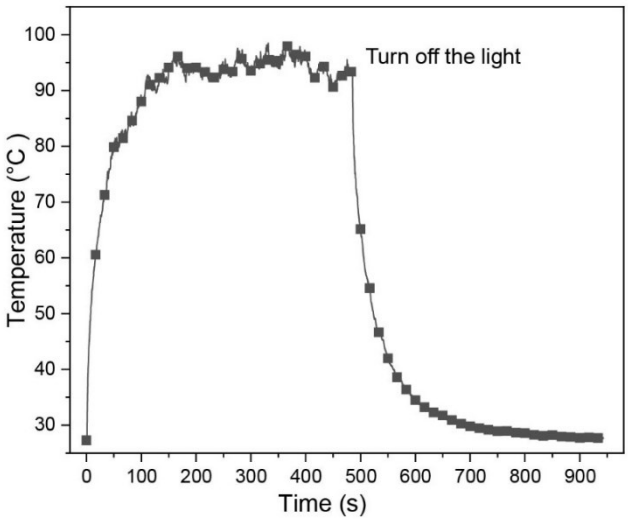

Fig. S11 Surface temperature curve of PPy/GFF in the dry state under one sun illumination on and off.

The surface temperature of the dry PPy/GFF rapidly increased from room temperature to ~90 °C within 100 s under one sun illumination, indicating an outstanding photothermal conversion ability.

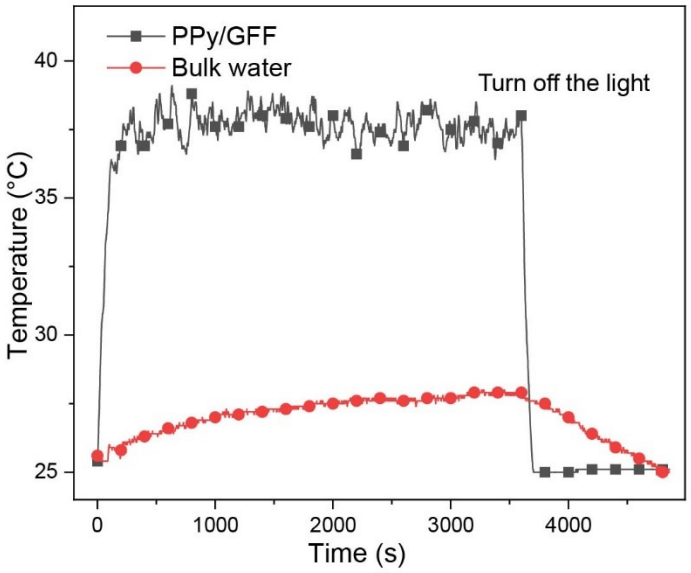

Fig. S12 Temperature variations with time for the PPy/GFF surface and the bulk water under one sun illumination on and off, respectively.

During the evaporation process, the surface temperature of PPy/GFF quickly rose up to the maximum value (~38 °C) while the temperature of the bulk water slightly increased with a slow rate because the interfacial evaporation strategy reduces the thermal conduction loss to the bulk water. This result demonstrates the outstanding photothermal conversion ability of PPy/GFF.

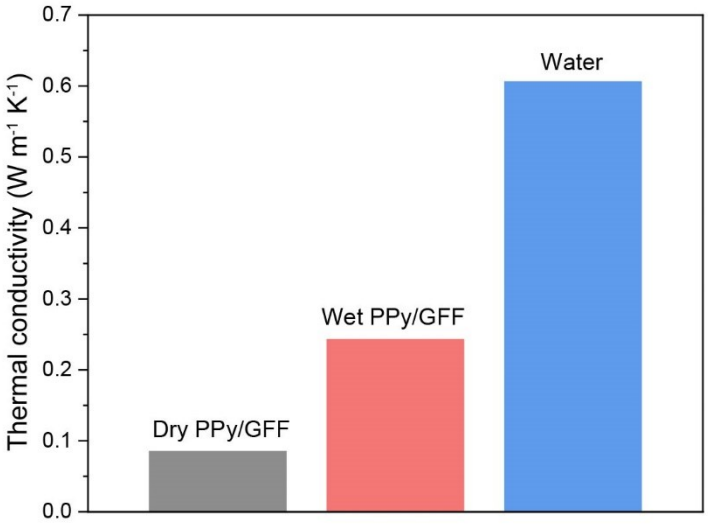

Fig. S13 Thermal conductivities of water and PPy/GFF in dry and wet state.

The measured thermal conductivity of PPy/GFF is 0.085 W m^{-1} K^{-1} and increases to 0.243 W m^{-1} K^{-1} in the wet state, still 60% lower than that of pure water (0.606 W m^{-1} K^{-1}).

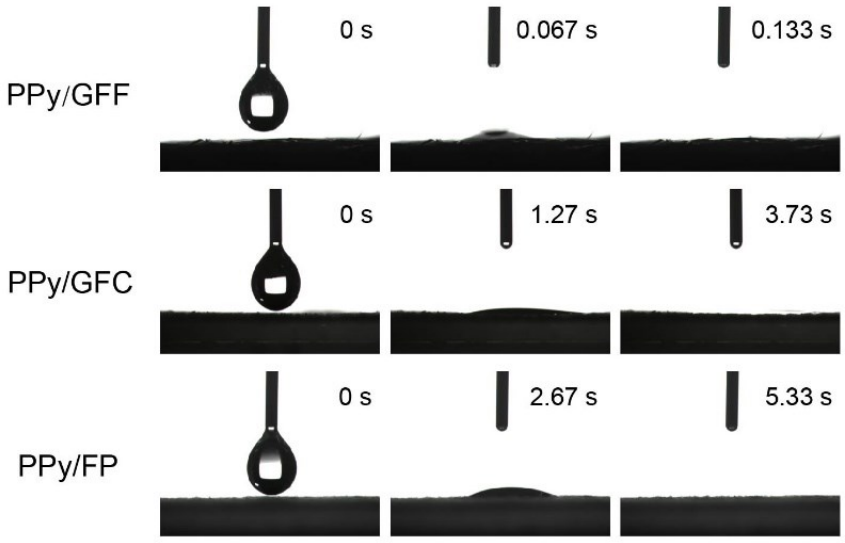

Fig. S14 Water contact angle measurement of PPy/GFF, PPy/GFC, and PPy/FP. The three snapshots taken in a row depict the fast transport of water droplet from the surface.

The water droplet completely diffused into the PPy/GFF within less than 0.13 s, demonstrating the extraordinary wettability and rapid water transport of PPy/GFF. This is attributed to the hydrophilic nature of PPy and abundant capillaries in the BCL structure of PPy/GFF. The fast water transport guarantees efficient water replenishment for evaporation and abundant pathways for salt dilution. The water transport in PPy/GFF is much quicker than that in PPy/GFC and PPy/FP, indicating a better water transport capacity.

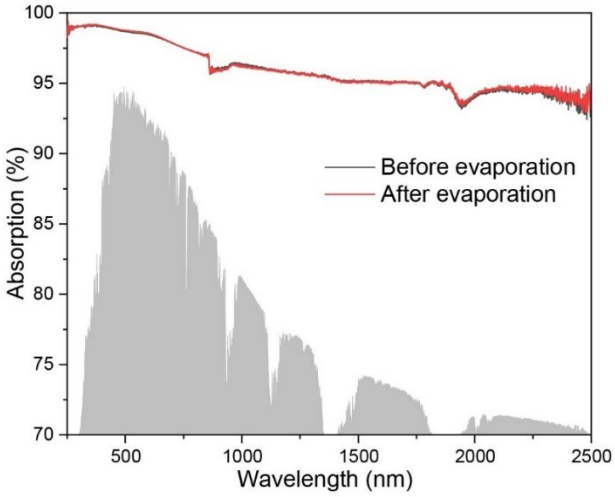

Fig. S15 Solar absorption spectrum of PPy/GFF before and after evaporation.

According to the solar absorption spectrum of PPy/GFF before and after evaporation, there is almost no change in the light absorption capacity of the sample due to its chemical and mechanical stability.

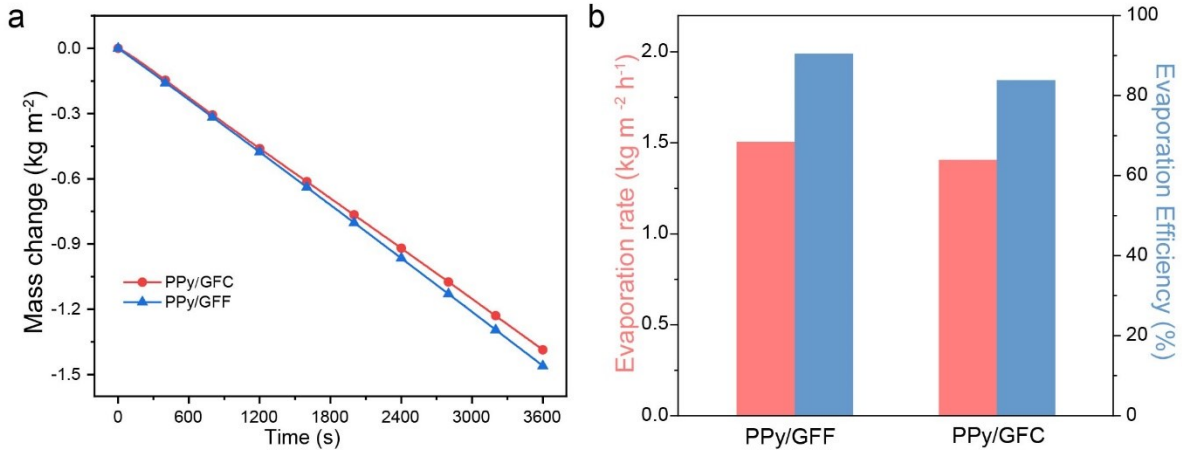

Fig. S16 Solar evaporation of PPy/GFF and PPy/GFC treating pure water under one sun irradiation. (a) Evaporation mass loss versus time curves. (b) Solar evaporation rates and efficiencies.

The control sample PPy/GFC shows a little slower evaporation rate (1.395 kg m^{-2} h^{-1}) than PPy/GFF. The calculated evaporation efficiency of PPy/GFC is 83.8%.

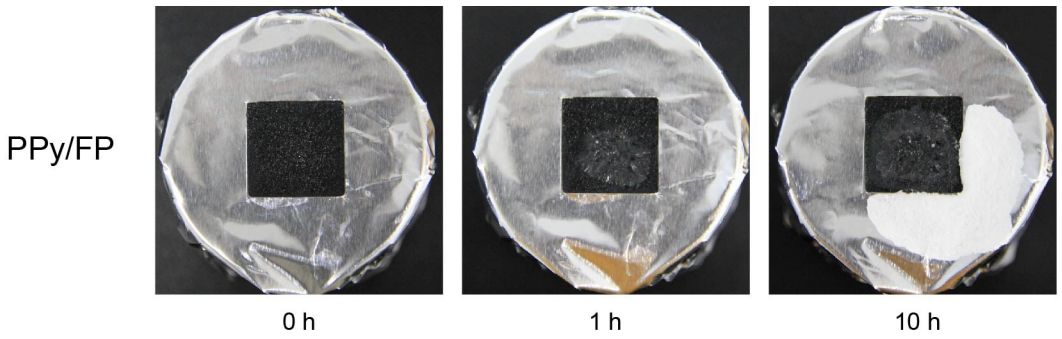

Fig. S17 Salt precipitation images of PPy/FP treating brine over 10 h under one sun irradiation.

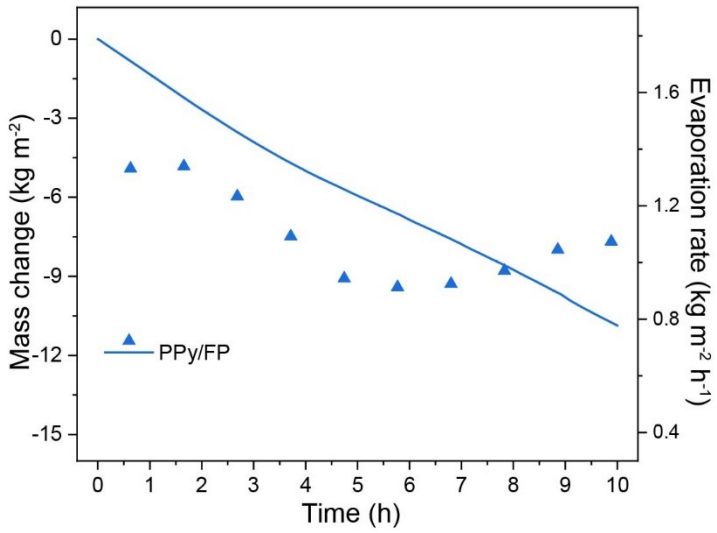

Fig. S18 Mass changes and evaporation rates of PPy/FP treating brine over 10 h under one sun irradiation.

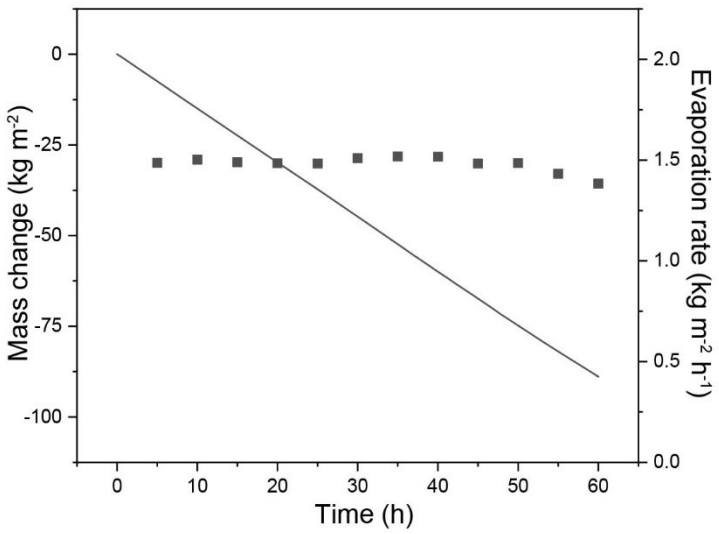

Fig. S19 Mass changes and evaporation rates of PPy/GFF treating brine over 60 h under one sun irradiation.

Fig. S20 Scheme of the bioinspired evaporator for solar steam generation.

The substrate applied here is a membrane with a square hole in the center. The absorber and fiber bundles are connected by chemical binder, constituting the whole evaporator. The absorber directly contacts with the air-laid paper for evaporation. The out terminal of salt secretion bundle is on the substrate so that the salt can keep creeping on the substrate.

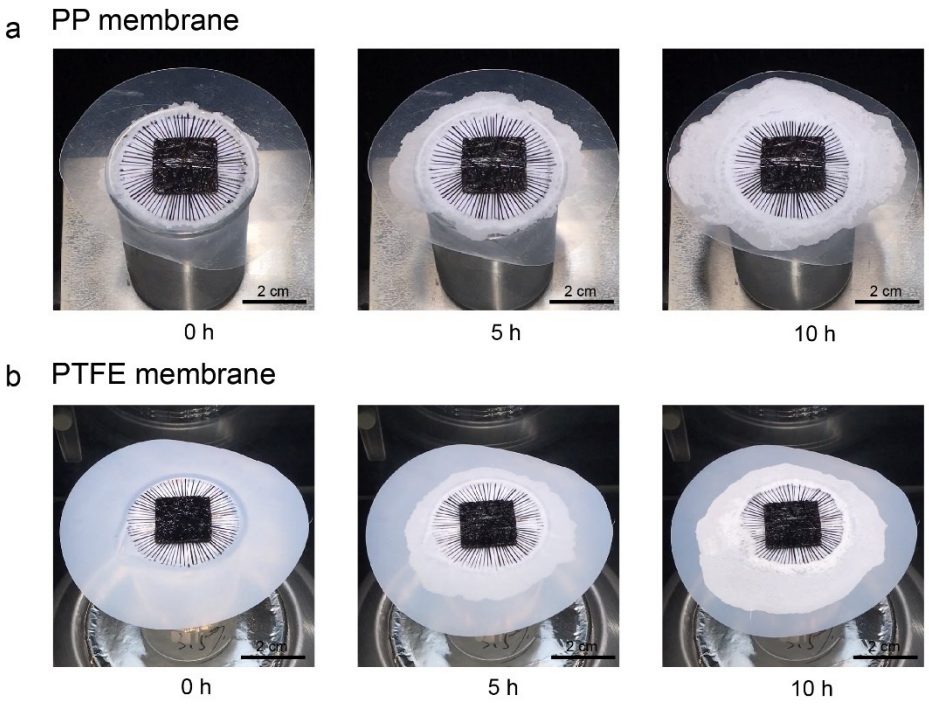

Fig. S21 Salt creeping on the PP membrane and PTFE membrane.

The substrate can be many materials, such as aluminum foil, PP membrane and PTFE membrane. The salt creeping mechanism can be applied to all these materials.

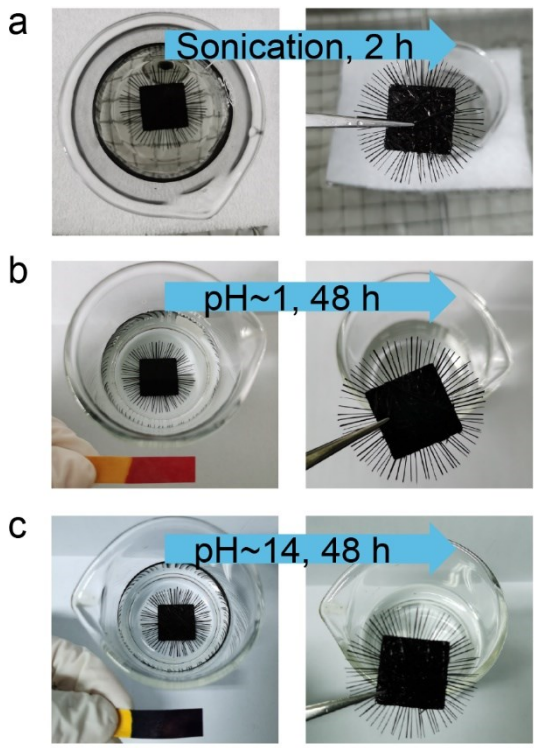

Fig. S22 Mechanical stability of the bioinspired evaporator under a series of harsh conditions. (a) ultrasonic agitation (200 W, 2 h), (b) acidic (pH~1, 48 h) and (c) alkaline (pH~14, 48 h).

The bioinspired evaporator maintained intact without any breakage after a series of harsh conditions.

Fig. S23 Optical images of salt creeping over time in the darkness.

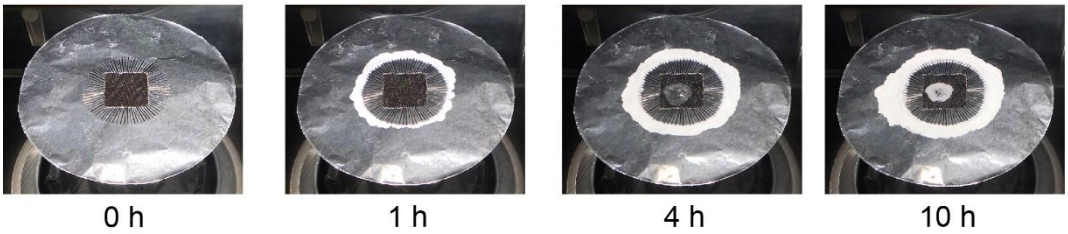

Fig. S24 Optical images of salt crystals forming over time for PPy/GFC with 80 bundles treating brine under one sun irradiation.

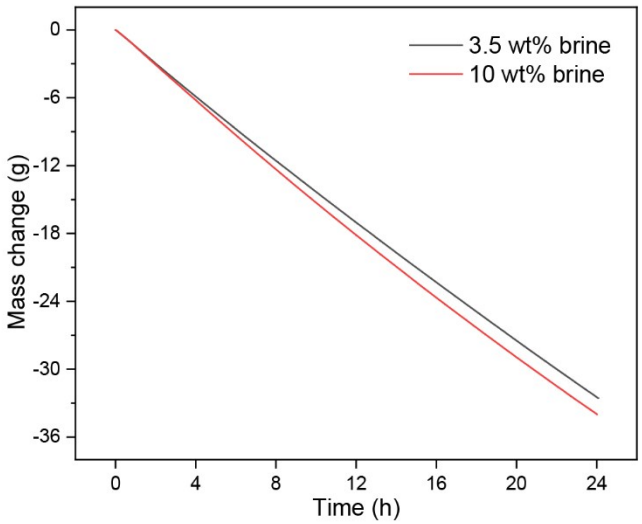

Fig. S25 Mass changes of the bioinspired evaporator treating 3.5 wt% and 10 wt % brine for ZLD over time.

Fig. S26 Optical images of the solar desalination prototype and water collection situation treating the artificial seawater with 3.5% salinity.

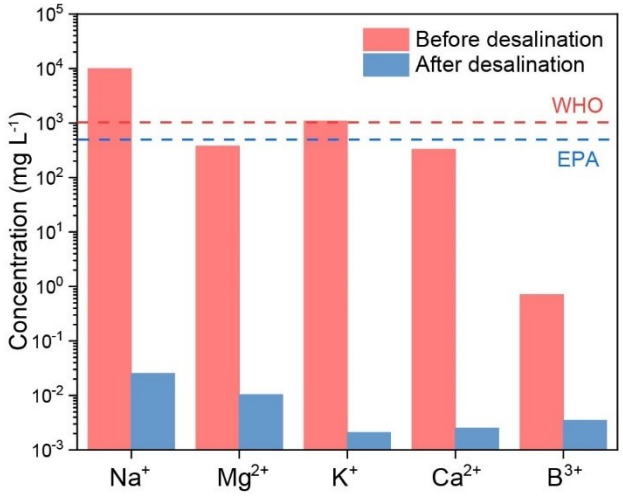

Fig. S27 Concentrations of five primary ions in artificial seawater before and after desalination, far below the lower limits of WHO and EPA standards for drinking water.

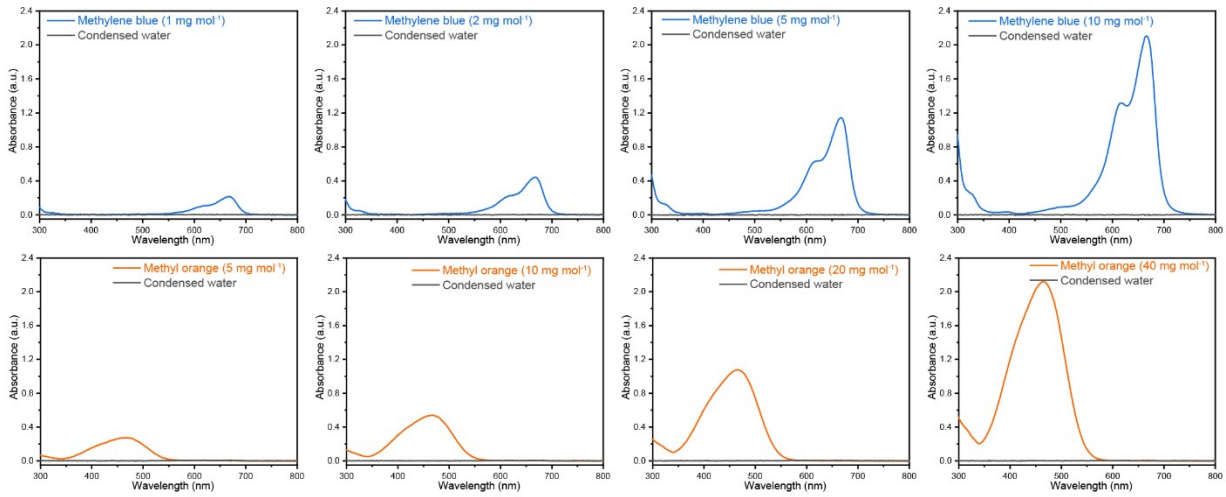

Fig. S28 UV-vis spectroscopy of the simulated sewage before and after desalination.

Methyl orange and methylene blue with different concentrations were utilized as the indicators of the pollutants to evaluate the purification effect of PPy/GFF. The UV-vis spectroscopy results show that there are almost no contaminants left in the all eight collected water samples.

Fig. S29 Quality tests of water from the Siyuan Lake (31.23° N, 121.48° E) before and after desalination.

The device successfully improved the quality of the water from Siyuan Lake by decreasing acidity and reducing organic and mineral contents.

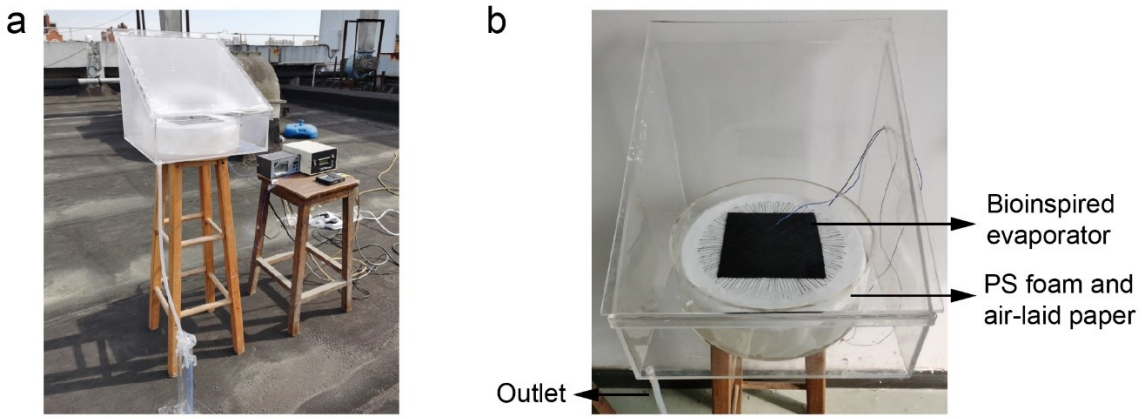

Fig. S30 Outdoor solar desalination. (a) Photograph of the outdoor solar desalination test. (b) Photograph of the solar still with the bioinspired evaporator.

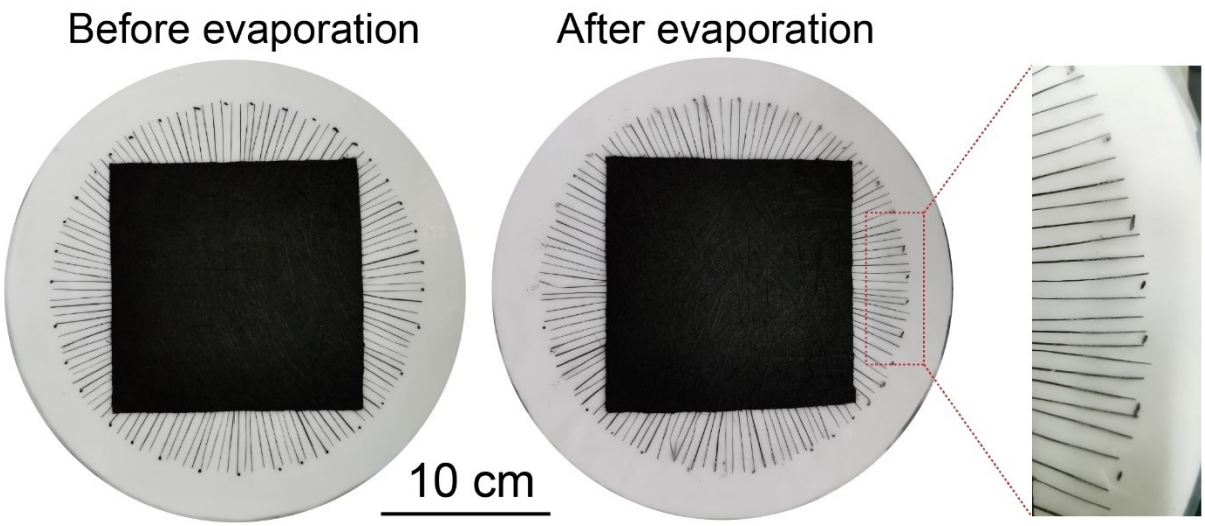

Fig. S31 Photos of the evaporator before and after the desalination.

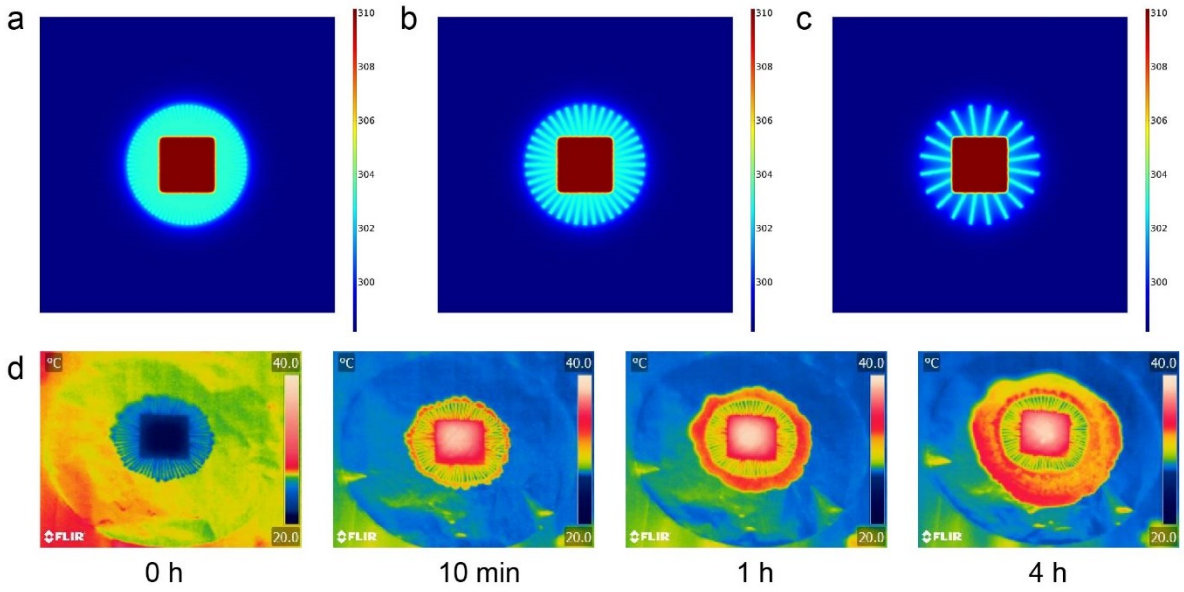

Fig. S32 Temperature profiles set in the simulation. (a-c) Surface Temperature profiles for 80-bundle (a), 40-bundle (b), and 20-bundle (c) configurations for the simulation, respectively. (d) Temperature profiles of the evaporator in the experiment over time.

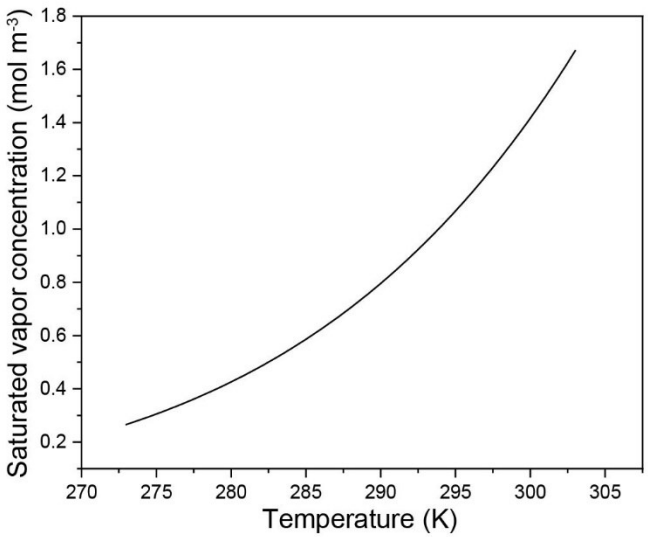

Fig. S33 Saturated vapor concentration with temperature.

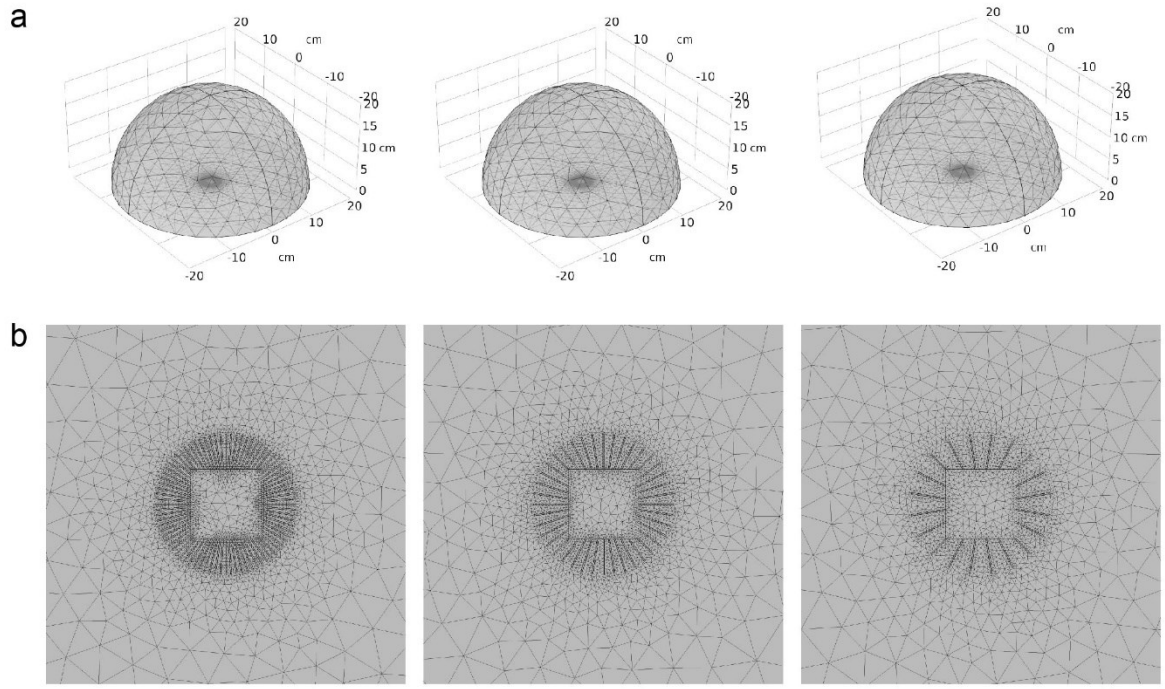

Fig. S34 Detailed geometrical conditions of the simulation for 80-bundle, 40-bundle, and 20-bundle configurations. (a-b) 3D (a) and 2D (b) Mesh layout of the simulation model.

The geometry is a hemisphere with a radius of 20 cm, much larger than the wet region. The mesh size is between 0.4 to 40 mm. Mesh is refined near the region of salt secretion bundles with the highest resolution. The environment parameters were set as the boundary conditions for the spherical surface of the hemisphere. The relative humidity of the environment is set to be 0.5. The environment temperature is set to 298.15 K.

Table S1. Cost estimation of PPy/GFF. (April,2020)

Chemicals	Vender	Price	Material consumption	Price/ material
Pyrrole	Aladdin	\$134.6 L^{-1}	1.1 ml	\$0.148
Iron (III) chloride hexahydrate	Aladdin	\$5.6 kg^{-1}	17.3 g	\$0.097
GFF	Jushi	\$0.85 m^{-2}	623.7 cm^2	\$0.053
Cost of PPy/GFF				**\$4.78 m^{-2}**

Table S2. The total enthalpy of liquid-steam phase change under different sun illumination.

Light intensity (kw m^{-2})	1	2	3	4	5	6	7
h_{LV} (kJ kg^{-1})	2466	2475	2480	2491	2502	2510	2515

Table S3. Summary of representative references on salt resistance treatment.

Ref.	Evaporation rate (kg m^{-2} h^{-1})	Solution (NaCl, wt%)	Continuous testing time	Price	Salt removing capability	Salt tolerance property	ZLD
14	2.5 kg m^{-2} day^{-1}	3.5	30 h	medium	/	/	/
15	1.26	25	120 h	high	√	/	/
16	1.3	3.5	0.75 h	high	/	√	/
17	2.5	3.5	96 h	high	/	√	/
18	0.8	15	7 h	low	/	√	/
19	1.04	20	100 h	low	/	√	/
20	1.42	3.5	600 h	high	√	/	√
21	1.28	10	8 h	high	/	√	√
22	1.46	3.1	12 h	high	/	√	/
23	2.63	25	9 h	high	√	/	/
This work	**PPy/GFF** 1.47	3.5	60 h	low	/	√	√
	Bioinspired solar evaporator	3.5 artificial seawater	600 h	low	√	√	√

Supporting Movies

Movie S1. Three-dimensional reconstructed image from the micro-computed tomography of PPy/GFF with X-ray microscopy.

Movie S2. Salt creeping phenomenon of 80-bundle configuration treating 3.5 wt% brine under one sun irradiation.

Movie S3. Brine transport and salt deposition when treating 20 wt% NaCl solution in the darkness.

Movie S4. Salt creeping phenomenon of 20-bundle configuration treating 3.5 wt% brine under one sun irradiation.

Movie S5. Salt creeping phenomenon of 40-bundle configuration treating 3.5 wt% brine under one sun irradiation.